Bio-inspired Compliance Grading Motif of Mortar in Nacreous Materials

Jabir Ubaid[a], Brian L. Wardle[b], and S. Kumar[a,c]*

[a] Department of Mechanical Engineering, Khalifa University of Science and Technology, Masdar Campus, Masdar City, P.O. Box 54224, Abu Dhabi, UAE

[b] Department of Aeronautics and Astronautics, Massachusetts Institute of Technology, Cambridge, MA 02139, USA

[c] James Watt School of Engineering, University of Glasgow, Glasgow G12 8LT, UK.
E-mail:

[*] Corresponding Author

Keywords: nacre, additive manufacturing, spatial material grading, bio-inspired materials, biomimicry

Abstract

The impressive toughness and strength of natural nacre, attributed to its multi-scale and -material hierarchical architecture, has inspired biomimicry and bio-inspired materials development, and here we show that material compliance gradients are a motif that can help explain their advantaged mechanical performance. We present experiments enabled via additive manufacturing that allow direct evaluation of a compliance grading motif of the mortar between the relatively stiff bricks of the nacreous material. Spatial grading of the mortar compliance redistributes stresses away from critical regions (at, and around, brick corners), resulting in overall increases of ~60% in strength, ~70% in toughness, and ~30% in strain-to-break, while maintaining macroscopic stiffness. Mechanistically, failure initiation threshold is delayed due to enhanced strain-tolerance and strain-localization as revealed in pre-failure experimental strain maps, and in agreement with numerical analyses. We further demonstrate that this modulus grading motif, beyond the stiffness mismatch between the brick and mortar periodic architecture, is a significant contributor to the performance

of the much-studied nacreous systems, and is suggested as a natural but overlooked mechanism in such systems.

Introduction

Nature is rich with many hierarchical and heterogeneous biological materials that concurrently exhibit outstanding mechanical properties such as high specific strength, high specific toughness and impact resistance[1-7]. These materials have evolved towards optimal system-level properties, including in some instances exceptional mechanical properties, which can be superior to those achieved by engineered materials[4, 6, 8-9].Focusing on mechanical properties such as those attributed to spider silk and nacre, the ultrahigh performance is credited to sophisticated hierarchical structures across multiple length scales together with advantaged spatial arrangement of the constituents consisting of different phases[4, 10]. Examples of such biological materials with exceptional structural motifs are bone, bamboo, wood, shell of mollusks and spider silk[4, 11-14]. Nacre is the iridescent material that is found in the shell of Abalone, a kind of mollusk. It is composed of 95 vol.% brittle mineral phase (aragonite ceramic) and 5 vol.% of a soft bio-polymeric matrix (proteins and polysaccharides)[6, 15-19]. Numerous investigations have revealed that nacre's microstructure resembles that of a brick-and-mortar architecture (see Fig. 1) where the stiff and brittle aragonite bricks are stacked and layered and the mortar acts as a compliant and energy dissipating bond between the bricks[15]. Despite having a primary brittle constituent, nacre possesses a desirable combination of properties such as toughness and strength, which are often antagonistic in practice[3, 5-6, 20-21]. As a result of its specific hierarchical composite architecture, the toughness of nacre is orders of magnitude higher than that of its major constituent-monolithic aragonite, while maintaining almost the same stiffness of the aragonite[6, 15, 22]. One of the key factors that govern the extraordinary toughness of nacre is sliding of the bricks (macroscopic work hardening) over neighboring bricks[6, 15, 23]. The relatively compliant and structurally weaker mortar undergoes localized deformation (yielding and work hardening) and fails locally causing macroscopic fracture (pull-out of bricks)[23]. A similar hierarchical structure can also be found in bone-a composite structure made of stiff inclusions embedded in softer matrix in a staggered pattern[4]. Both nacre and bone exhibit several toughening mechanisms such as crack deflection, micro-cracking, crack bridging and other energy dissipation modes operating at different length scales[21, 24-25]. The identification of individual mechanisms is ongoing, with much recent progress focused on nanometer-scale constituents and particular molecular arrangements[26-27].

Understanding the biological engineering of nacre and other biomaterials is ongoing, and here we focus on a relatively simple, but overlooked and impactful, motif in nacreous systems: spatial compliance grading motifs (CGMs) of the compliant mortar. Such CGMs are observed in many biological materials such as elasmoid fish scale[28-29], spider fang[30], byssal thread[31-32], horse hoof[33-34] and squid beak[35-36]. The outstanding properties of biological materials and their ability to inherit the beneficial properties of their constituents while dispensing their detrimental properties[4, 25, 37] have inspired researchers to emulate the structural motifs of these materials in order to engineer materials with enhanced performance. Though, various studies have shown that remarkable improvements in material properties can be achieved via bio-inspired strategies[4, 9, 25, 37-49] including spatial gradients in material property and/or morphology[47-49], none of the experimental studies has thus far considered the CGM widely found in many natural materials. Several routes available to synthesize bio-inspired composites include large-scale layered composites, hot press assisted slip casting, ice templation, freeze casting, bio-mineralization and self-assembly[6, 37, 39]. Additionally, the latest advancements in additive manufacturing (AM, aka 3D printing) have opened a flexible and accurate way to integrate multiple materials of contrasting material properties into a composite structure in a single build at micrometer resolutions[11, 50-51]. This, together with emerging advances in nanoscale AM empowers multi-material AM as a suitable tool for the creation of bio-mimicking structures[51-52].

Recent experimental studies fabricated nacre-inspired structures via AM and the performance quantified in relation to the constituents[20, 37, 43, 50]. Several recent studies demonstrated enhanced mechanical response under quasi-static tension[20, 53-54], damping characteristics under cyclic tension[55] and low velocity impact resistance[56] of AM-enabled nacreous materials. In such nacreous structures, a large stiffness mismatch (e.g. modulus ratio of ~1500 and ~3000 [53-54]) between the brick and mortar is engineered to facilitate dissipation of energy through the complaint mortar layer. Nevertheless, the stress distribution in the mortar is non-uniform with high stress gradients and localized stress concentrations around the corners of the bricks[57-58]. These regions of high stress concentration are oftentimes sites of failure initiation and we postulate that CGMs in the mortar of nacre, apart from the bulk stiffness mismatch between the brick and mortar, play a role in toughening and strengthening the nacreous system (similar to compliance gradients found in nature). Spatially tailoring the elastic stiffness of the mortar such that the compliance of the mortar in the zone of stress concentration is lower than that away from stress concentration zones will enhance strength and toughness. Such spatial compliance grading of mortar in either discrete-steps or smoothly varying (more akin to nature) diffuses the stresses and moves the concentration away from the potential sites of failure initiation, imparting strain tolerance.

Numerous studies have demonstrated the use of AM to realize nacre-like physical models[11, 41, 55, 59-65]. Their performance is governed by multiple factors: stiffness mismatch between the brick and mortar, aspect ratio of the overlap region between two neighboring bricks, periodic arrangement of structural elements, hierarchical architecture, and the volume fraction of the bricks in the nacreous material[23, 55, 66]. The geometric and the material properties (both mono- and multi-layer models have been employed) of the nacre must be chosen such that the shear stress distribution in the mortar is quasi-uniform over the overlap length[23]. A non-dimensional elastic shear transfer number[23], β_0, is typically employed to determine the nature of shear stress distribution in the mortar of nacreous system, given by

$$\beta_0 = \rho_0 \sqrt{\frac{G_m}{E_b} \frac{w_b}{w_m}} \tag{1}$$

where, ρ_0 is the overlap length ratio given by $\rho_0 = \frac{2l}{w_b}$ (see Supplementary Fig. 1 and Supplementary Table 1). G_m and E_b are the shear modulus of mortar and Young's modulus of brick respectively. w_b and w_m are the widths of brick and mortar respectively. Herein, in addition to other geometric and material properties, compliance of the baseline mortar (ungraded) of the nacreous materials is chosen such that the shear stress distribution is quasi-uniform along the overlap length to match the behavior of natural nacre. The mortar chosen here is nearly incompressible (Poisson's ratio $= \frac{1}{2}$), which renders $G_m = \frac{E_m}{3}$, and the elastic shear transfer number can be recast as:

$$\beta_0 = \rho_0 \sqrt{\frac{1}{3} \frac{E_m}{E_b} \frac{v_b}{v_m}} \tag{2}$$

where E_m is the modulus of mortar. v_b and v_m are the volume fractions of brick and mortar in the nacreous material, respectively. For smaller β_0 values ($\beta_0 \approx 1$ or smaller), shear stress distribution in the horizontal mortar is quasi-uniform along the overlap length. For larger β_0 values, steep gradients of shear and peel stresses occur at the overlap ends causing premature failure inconsistent with natural nacre. For the geometric and material parameters used in this study (see Supplementary Table S1 and S2), the elastic shear transfer number β_0 is calculated to be 0.12, indicating that proper quasi-uniform shear stress distribution is achieved as in natural nacre. Numerical models are utilized to study the effect of step-wise spatial compliance grading of the mortar (see Fig. 1b) on the stress distribution in the structure and design graded solutions for experimentation. Realization of model nacreous structures is achieved using multimaterial polymer AM, followed by macroscale testing to assess the effects of the hypothesized motif of compliance gradients in the mortar on the mechanical performance of the nacreous materials.

Results and Discussion

Baseline (ungraded) and graded nacreous specimens are experimentally realized and tested to failure in tension. A tough nacre-like response from the AM specimens with two-layer brick-mortar structure, designed as discussed in the introduction utilizing appropriate volume fractions of constituents and the non-dimensional elastic shear transfer number β_0, is observed in preliminary mechanical testing of ungraded nacreous structures whose geometrical details are given in Supplementary Fig. 1. The load-displacement response of these nacreous structures for different choices of mortar material i.e., $E_b/E_m = [3309,\ 2044,\ 1468,\ 834]$ and non-dimensional elastic shear transfer number, $\beta_0 = [0.079, 0.1001, 0.1187, 0.158]$ respectively is shown in Supplementary Fig. 2. Note that the tensile response of the AM-realized brick-and-mortar nacre-like structures shows two load peaks, exhibiting significantly improved toughness, relative to homogeneous plates (see Supplementary Fig. 3). These results are consistent with other studies of nacre utilizing AM-enabled physical models[43, 53].

Two compliance grading schemes are experimentally realized and tested, to compare with the baseline ungraded case, as shown in detail in Supplementary Fig. 4 (and conceptually in Fig. 1) together with the variation of Young's modulus. In both schemes, the compliance of the isotropic mortar is varied in the loading direction around the corners of the bricks in discrete step(s) as shown in Fig. 1 and Supplementary Fig. 4. In the single-step grading scheme, the mortar modulus is reduced from E_m to E_{mA} in region-A at the end of the bricks, of length equal to the width of the mortar (see Fig. 1). In the double-step grading scheme, the mortar modulus is reduced in two discrete steps (*i.e.*, from E_m to E_{mB} at region-B of length l_B and it is further reduced to E_{mA} at region-A). Working within the palette of available AM materials, Shore50 ($E_m = 1.42$ MPa, $E_b/E_m = 1468$) is used for the baseline mortar. Note that tailoring the mortar compliance in this way maintains or improves the quasi-uniform shear transfer mode discussed earlier – see discussion and equations (1) and (2). By tuning the compliance of the horizontal mortar spatially, particularly near the corners of the bricks where the stress is concentrated, strain-tolerance is imparted without altering the global stiffness of the nacreous system (as can be seen in Supplementary Fig. 5, Supplementary Fig. 6 and Table 1). Maintaining stiffness is critical for a complete comparison of the mechanical performance. Figure 2 shows the experimentally realized representative load-displacement response of the baseline and graded specimens together with optical images corresponding to the first and second load peaks, representing vertical mortar failure and horizontal mortar (as well as complete) failure, respectively. Immediately after the first peak, the load-transfer between bricks begins to wholly occur through the horizontal bridges, exhibiting a work-hardening type response, as observed by others in nacreous-system modeling and experiments[43, 53]. With further loading, the resistance increases to a maximum (corresponds to a global maximum in the load-displacement curves, see Fig. 2b) where pull-out failure of the bricks occurs along the horizontal mortar. The results indicate significant improvement in strength (+62 % for single-step grading, and +65 % for double-step grading) and modulus of toughness (+ 68 % for single-step grading and +71% for double-step grading) of graded structures compared to the tough baseline nacre, with negligible change in the initial stiffness and the load at first peak (see Table 1). Synchronized video of the load-displacement response and the corresponding optical images of the samples provided in Supplementary Video 1 shows the failure progression just described. Additionally, Fig. 3 shows deformation and damage evolution maps of the samples at different of stages of loading (as indicated in the load-displacement response shown in Fig. 2). Figure 3a shows the failure of the vertical mortar that corresponds to the first peak in the load-displacement response. Subsequent strain hardening coupled with damage accumulation is clearly visible in Fig. 3b and 3c during which the load transfer between bricks wholly occurs through shearing, leading to failure of the horizontal mortar, corresponding to the second peak in the load-deflection response as seen in Fig. 3d. After the horizontal and vertical mortar failures, final failure is localized near the sample free edge in all cases. The optical images corresponding to final failure of the samples are shown in Fig. 3e, showing the deflection of cracks into the mortar. All three sample types fail in a self-similar fashion having the same trajectory and modes of failure in the same order, however, the CGM samples delay failure of the horizontal mortar due to the strain-tolerance engineered via the local increased compliance at the brick ends. 2D surface strain fields for the samples calculated at a load of 90N (slightly lower than the first peak) using digital image correlation (DIC) technique is presented in Supplementary Fig. 5 (lower resolution) and Supplementary Fig. 6 (higher resolution). The strain field indicates increased strain-tolerance (higher strains in the graded regions) and strain-localization in the nacreous structures due to the compliance gradients. DIC results show 28%, 29% and 19% increase in maximum longitudinal strain (ε_{xx}), peel strain (ε_{yy}) and shear strain (ε_{xy}) respectively due to compliance grading of the mortar (see Supplementary Fig. 6 and Supplementary Table 3), as expected. Note that these strain maps are evaluated before the first failure to correspond with the numerical results for the CGM design.

To understand the stress-transfer between bricks through the mortar, finite element (FE) analysis of the ungraded baseline nacreous structure with Shore50 ($E_b/E_m = 1468$) as the mortar material, is conducted and the stress distribution around the corners of the bricks in the mortar is analyzed. The stress distribution in the horizontal and vertical layers of the mortar are shown in Fig. 4b before the first peak (~ 90 N, see Fig. 2b). On the left side of Fig. 4b is the stress distribution in the horizontal mortar at the midline of the top brick-mortar structure layer and near the brick-mortar interface (0.15 mm from the interface) along the length of the unit cell (L), while the right side of Fig. 4b shows the stress distribution in the vertical mortar at the midline of top brick-mortar structure layer and near the brick-mortar interface (0.15 mm from the interface) along the width of a brick (see Supplementary Fig. 7 for lines of stress extraction). During the early stages of loading, tensile stresses in the vertical bridges are dominant, i.e., the longitudinal stress, σ_{xx} dominates the stress-state and the magnitude of the shear stress, σ_{xy} is small compared to the longitudinal stress, while the peel stress, σ_{yy} is compressive. Therefore, the longitudinal stress (tensile) dictates the failure of the vertical mortar (represented by the first peak in load-displacement curves shown in Fig. 2b). As shown in Fig. 4b, the magnitudes of the different stress components in the horizontal mortar are comparable before the first peak, exhibiting a complex tri-axial stress-state. From the FE analysis, stress concentrations and steep gradients are observed in regions close to the horizontal and vertical mortar junctions, which lead to failures of the nacreous material.

To shed light on change in stress-transfer behavior of the CGM nacreous structures, FE analyses of all experimentally realized baseline and graded cases are performed and the normalized longitudinal, peel, shear and equivalent stress distributions in the horizontal mortar (of the baseline and graded structures) over the length of a unit cell (at the middle z-plane of a brick-mortar structure but near the brick-mortar interface) under a tensile load of 90 N are presented in Fig. 5 (see Supplementary Fig. 1 for geometric details and Supplementary Fig. 7 for lines of stress extraction). As can be seen, the engineered strain-tolerance via compliance grading of the horizontal mortar has favorably redistributed the stresses in the mortar and has diffused the peak stresses, delaying the onset of failure. Significant reduction in the stress peaks obtained for the longitudinal, peel and shear stresses are summarized in Table 2. Stress peak reduction is relatively larger for double-step grading than for the single-step grading, as expected. Supplementary Video 1 and Fig. 3 show that the failure initiation in horizontal mortar begins near the corners of the bricks from the outer edges of the samples where the bricks are less constrained (i.e., prone to bending), experiencing high peel stresses. This indicates that the failure initiation of the horizontal mortar occurs predominantly due to peel stresses. FE analyses of experimentally realized graded cases indicate that the reduction in peak peel stresses for single-step and double-step grading schemes is almost the same (difference of ~5%). Therefore, the nearly identical experimental performance of single-step and double-step graded structures is attributed to the same extent of peel stress reduction in both grading schemes employed. Thus, despite significant reductions in shear and longitudinal stress concentrations due to the double-step grading, the dominance of the peel stresses in the observed failure do not evidence further improvement from the double-step tailoring over the single-step as this stress is not additionally reduced significantly from the single- to the double-step.

These significant improvements in load-carrying capacity suggest that material property gradients, such as the CGM of mortar introduced here, can help explain advantages of the much-studied nacreous system via the new CGM designs. Additional performance enhancement should be possible with more sophisticated grading schemes (such as smoothly and nonlinearly varying mortar and/or brick compliance) than those realized here experimentally. To investigate the potential of additional property variation beyond what could be experimentally realized in this work to improve the nacreous system, a number of linear FE analyses are performed by varying the material properties of both ungraded and graded structures with the same criterion of reduced stress concentration used in designing the single- and double-step tailoring schemes, and analyzing the experimental results. The combinations of material properties (which can't be realized via 3D printing) that produce the most desirable stress-state (as defined by lowest peak stresses) in the nacreous structure are identified. FE analyses are initially conducted for ungraded nacreous structures varying the moduli mismatch between of the bricks and the mortar (E_b/E_m) from 1 to 6000, while keeping the brick aspect ratio ($\bar{b} = l_b/t$) and overlap length ratio ($\bar{l} = 2l/l_b$) constant. The choice of $\bar{b} = 10$ and $\bar{l}$ =0.48 enables retention of a quasi-uniform shear stress distribution in mortar. Supplementary Figure 8 shows the normalized peak longitudinal, peel, shear and equivalent stresses in the mortar for different choices of E_b/E_m. As the E_b/E_m ratio increases from 1, the stress-state in the mortar changes from simple tension to a complex tri-axial stress-state (consistent with the stress states evaluated for the baseline nacreous system) evidenced by the increase in peak peel and shear stresses, and a decrease in peak longitudinal stress. Further increase of E_b/E_m from 250 is found to have negligible effect on the mortar peak stresses. For the subsequent analyses, we therefore use $E_b/E_m = 500$. We further continued FE analyses for single-step compliance graded structures (see Fig. 1) by keeping $E_b/E_m = 500$ and varying the ratio of modulus of mortar and modulus of region-A of the mortar, E_m/E_{mA}. The normalized peak longitudinal, peel, shear and equivalent stresses in the mortar for different choices of E_m/E_{mA} are shown in Supplementary Fig. 9. It can be observed that as E_m/E_{mA} increases from 1, the peak stresses reduce considerably, but further increase of E_m/E_{mA} over 100 has negligible effect on the peak stresses. A value of 100 is therefore chosen for E_m/E_{mA} for subsequent FE analyses. Double-step compliance graded structures are analyzed by varying the ratio of modulus of mortar and modulus of region-B (E_m/E_{mB}) as well as the length of region-B (indicated by l_B/l-the ratio of length of region-B, l_B and the length, l as shown in Supplementary Fig. 4). Analyses were performed by keeping $E_b/E_m = 500$ and E_m/E_{mA} = 100. Peak normalized stresses for different choices of E_m/E_{mB} as a function of l_B/l ratio are shown in Supplementary Fig. 10. For $l_B/l \leq 0.5$, the lowest peak longitudinal and peel stresses can be seen for $E_m/E_{mB} = 35$ at $l_B/l = 0.4$ while for all other cases, minimum peak stresses occur at $l_B/l = 1.0$ for $E_m/E_{mB} = 50$. The trend is different for peak shear stresses: except for lower l_B/l values, peak shear stresses increase as l_B/l increases from 0 to 0.8 and reduces when l_B/l increases further from 0.8. It can be observed that a l_B/l ratio of 0.4 and E_m/E_{mB} value of 35 give a desirable stress-state, reducing peak longitudinal and peel stresses by over 70% with a concomitant minor increase in peak shear stress (≅ 4%) compared to the single-step grading scheme ($l_B/l = 0$) and the case where l_B/l = 1 (the region-B with modulus E_{mB} everywhere in the horizontal mortar except for the region-A). As noted earlier, peel stress reduction is most strongly correlated with overall performance enhancement in the experiments. Note that the peak stresses are the lowest for $l_B/l = 1.0$ but this choice may not have enough stiffness to efficiently transfer load between the bricks and is therefore not considered. Thus, the parametric FE studies indicate that for a different choice of modulus gradient(s), different to those realized experimentally, higher reduction in peak peel stresses (shown to dominate first failure in the experimental work) can be achieved, up to a 70% reduction vs. the ~30% reduction noted in the single- and double-step CGM realized here experimentally. These predicted higher-performance CGM designs are not experimentally realized due to the limited choice of material options available for multimaterial 3D printing. The parametric finite element studies presented here can be considered preliminary and not an optimization due to both the material linearity assumption and the focus on peak stresses in this region, but is instructive to show even further advantage beyond the two (single and double-step) compliance grading schemes considered here, *i.e.*, the CGM is clearly significant and potentially dominant in the mechanics of nacreous materials.

Conclusions

Nacre, although comprised primarily of a brittle "brick" constituent, concurrently exhibits extraordinary strength and toughness, due to several noted and studied features including its periodic and hierarchical microstructures, and nanostructured composition. Here, we reveal that spatial compliance gradients in the compliant "mortar" between the bricks is a new motif that contributes to nacreous materials' advantaged mechanical properties. Herein, we have realized nacreous structures with CGMs of mortar via multimaterial AM. Performance measurement of compliance graded nacreous materials reveals ~60% improvement in strength, ~70% in toughness, and ~30% in strain-to-break, while importantly retaining the macroscopic stiffness. The enhanced tensile behavior of the CGM nacreous materials suggests that engineered strain-tolerance via spatial compliance gradients improves work hardening, leading to enhanced strength and toughness. Numerical models of the experimentally realized graded schemes indicate an ~30% reduction in peak peel stresses from the baseline non-graded case, which primarily dictates the failure. Numerical parametric studies of graded structures reveal that further improvements can be achieved with other ratios of compliance mismatch in the single- and double-step grading configurations considered here: over 70% decrease in peak peel stress is observed for compliance grading schemes that produce desirable stress-states in the initial linear response regime, more than doubling the peel stress reduction of the experimentally-realized CGMs herein. CGMs of mortar in nacreous materials with strongly spatially varying compliance can allow them to be engineered with stiff, tough, and damage tolerant properties and our results suggest that the mechanical performance (here, tensile, but performance evaluation under bending and other loadings is left to a subsequent study) can be further enhanced via bio-inspired spatial compliance motifs in one or more phases of the nacreous material, *e.g.*, CGMs in vertical mortar. Emerging advances in nanoscale AM that enable spatial compliance grading of the materials at micro and nano-length scales in conjunction with bio-inspired compliance grading of periodic and hierarchical structures could lead to development of next-generation high-performance multifunctional materials with unprecedented mechanical properties.

Materials and Methods

Finite element analysis to design the nacreous structures for 3D printing is described, followed by the experimental specifics, including 3D printing and mechanical testing procedures. Geometric and material properties are chosen to ensure quasi-uniform shear stress-state in the mortar (as discussed above) and are further detailed below. The geometric parameters of AM-enabled nacre (see Supplementary Fig. 1) are: $l_b = 20\,mm$ and $w_b = 2\,mm$, and mortar thickness $w_m = 0.8\,mm$ with brick aspect ratio, $\bar{b} = l_b/w_b = 10$ and overlap length ratio, $\bar{l} = 2l/l_b = 0.48$.

Finite Element Analysis

Numerical analysis for the nacreous structures were performed using Abaqus/Standard FEA Version 6.12. A 3-dimensional linear-elastic finite element model was created using 8-node linear brick elements (C3D8) and all the geometric parameters matched the experimentally realized and tested specimens. The linear-elastic finite element analysis is performed to understand the effect of different compliance grading schemes on strain and stress redistribution in the linear elastic regime (where the nacre, as a structural system, should spend effectively all its life), to make rational choices about the form of the CGMs, and not to predict the failure and toughness of the system. Failure prediction would involve nonlinear constitutive and damage modeling of all the digital materials used in the AM system and is beyond the scope of this investigation. A mesh convergence study was conducted on the nacreous structure which showed that refining the mesh below a mesh size of 0.15 mm has little effect on the stress distribution in the mortar, near the mortar – brick interface (less than 1 % change in the peak stresses). The entire model is meshed with an element size of 0.1 mm. Material properties obtained from the mechanical tests of dogbone samples (see Supplementary Fig. 11 and Supplementary Table 2) are used for the finite element analysis. The y planes and z plane of the tabs that pass through the center of the tabs are constrained in y and z directions, respectively, with one side subjected to a tensile stress, σ_∞ as shown in Fig. 4a.

3D Printing and Mechanical Testing

Nacreous structures explored in this study are fabricated using multimaterial AM of photopolymers. The CAD models of the samples are created using Solidworks (Dassault Systems, France) and an Object Connex260 3D printer (Stratasys Ltd., USA) is utilized to fabricate the samples. This multimaterial 3D printer utilizes polymer jetting technology and builds parts layer-by-layer on the print tray by dispensing the liquid polymer through the print head nozzles. The jetted photopolymers are effectively instantly cured by the UV light from a UV lamp housed in the print head. The printer has a resolution of 16 μm in the z- direction (out of the build plane) and 42 μm in the x- and y- directions (in the build plane)[67]. The printer uses a polymeric support material named Objet Support SUP705 that helps to attain desirable surface finish and also to print overhanging structures. In order to avoid the effect of printing direction on the mechanical properties of the printed structures, which is a common and noted issue with such 3D printed parts, all samples are printed in the same x- direction.

Two acrylic based photopolymers, VeroWhitePlus^{TM} RGD835 and TangoPlus FLX930, which exhibit contrasting mechanical properties are used in this study. VeroWhitePlus^{TM} RGD835 is a stiff polymer (Young's modulus E_b=2,085 MPa) and TangoPlus FLX930 is a soft rubbery material (E_{mA}=0.63 MPa). The printer is capable of combining the two polymers in varying proportions to produce a range of materials with intermediate properties called digital materials. Structures with spatially varying material properties can be fabricated by using the two base polymers and/or the digital materials. First, homogeneous dogbone samples of all the material combinations explored in this study are printed and their constitutive properties are individually evaluated. The elastic properties of the different materials, including the digital ones used in this study are given in Supplementary Table 2 and their constitutive response is shown in Supplementary Fig. 11. The wide range (4 orders of magnitude, from 0.63 to 2,085 MPa) of elastic moduli of these materials makes them suitable for the fabrication of nacreous materials with spatially varying compliance of the mortar. The smallest geometric feature of the nacreous structure fabricated is 0.5 mm which is over an order of magnitude larger than the printer's resolution given above. The geometrical features of the nacreous structure are shown in Supplementary Fig. 1 with values given in Supplementary Table 1. One-layer and two-layer brick-mortar structures were fabricated and experimentally evaluated. The layers in the two-layer brick-mortar structure are arranged in a staggered pattern in both the x- and y- directions to each other together with an intervening mortar layer. The load-displacement response and optical images corresponding to the first and second peaks of baseline and graded one-layer samples are shown in Supplementary Fig. 12 and the results are summarized in Supplementary Table 4. We find that the mechanical performance of two-layer structure (discussed in the results section) is superior to that of the one-layer structure due to the enhanced load transfer enabled by an intervening layer between the two layers of brick-mortar structure. The baseline of two-layer nacreous structure has a maximum load (150.03 N) that is 408% higher than the maximum load of one-layer baseline case (30.6 N). Thus, our study concentrates primarily on the two-layer structure, as it also exhibits periodicity in z direction as in natural nacre. For ungraded cases, the bricks are printed using VeroWhite, E_b=2,085 MPa and the mortar is printed using Shore50-a relatively complaint digital material with elastic modulus, E_m=1.42 MPa. For graded nacreous structures, the compliance of the mortar is varied (increased) in the stress concentration zone (at and around the corners of the bricks) to diffuse the stress concentrations. The two compliance profiles (single-step and double-step) of the mortar that are experimentally realized and tested are shown in Fig. 1. In single-step grading, region-A (see Supplementary Fig. 4) is printed with TangoPlus (the most compliant polymer) having a modulus, E_{mA}= 0.63 MPa, and for the double-step grading, region-A is printed with TangoPlus and region-B (see Supplementary Fig. 4) is printed with Shore40 – a digital material with modulus E_{mB}=1.02 MPa, enabling spatially graded designs by varying the mortar's properties in fine discrete steps. Together with nacreous structures, grip spacers are printed with VeroWhite having modulus of 2080 MPa in order to clamp the samples for the mechanical testing as described in the supplementary information, section S2.

Mechanical testing of the dogbone samples and nacreous structures are performed using a Zwick-Roell mechanical testing machine. A 2.4 kN load cell with an accuracy of better than ± 0.25 % for the measurement range of 10 to 2500 N is used. Tensile load in the longitudinal direction of the sample is applied at a crosshead speed of 5mm/minute while the displacement is measured with a travel resolution of 0.04 μm at the grips, i.e., crosshead displacement. Digital image correlation was performed on dogbone samples and on the nacreous structures. A random speckle pattern was generated on the specimen surface by spraying white and black color acrylic paints using an air brush. Images of the speckled specimen surface were captured using a 5.0 MP monochrome camera and Vic-snap software (Version 8, Build 489) at 1 Hz. Vic-2D software was used to analyze the images of the speckle pattern and evaluate the 2D strain field of the specimen surface. In order to ensure the repeatability of results, 3 samples of each case were fabricated and tested. From the load-displacement response obtained from the mechanical tests, initial stiffness, load at first peak, maximum load, deflection at break and modulus of toughness are calculated along with standard error on all measured values.

References

(1) Gu, G. X.; Takaffoli, M.; Hsieh, A. J.; Buehler, M. J. Biomimetic Additive Manufactured Polymer Composites for Improved Impact Resistance. *Extreme Mechanics Letters* **2016,** *9*, 317-323.

(2) Tran, P.; Ngo, T. D.; Ghazlan, A.; Hui, D. Bimaterial 3d Printing and Numerical Analysis of Bio-Inspired Composite Structures under in-Plane and Transverse Loadings. *Composites Part B: Engineering* **2017,** *108*, 210-223.

(3) Huang, Z.; Li, H.; Pan, Z.; Wei, Q.; Chao, Y. J.; Li, X. Uncovering High-Strain Rate Protection Mechanism in Nacre. *Scientific reports* **2011,** *1*, 148.

(4) Studart, A. R. Biological and Bioinspired Composites with Spatially Tunable Heterogeneous Architectures. *Adv. Funct. Mater.* **2013,** *23* (36), 4423-4436.

(5) Launey, M. E.; Munch, E.; Alsem, D.; Barth, H.; Saiz, E.; Tomsia, A. P.; Ritchie, R. O. Designing Highly Toughened Hybrid Composites through Nature-Inspired Hierarchical Complexity. *Acta Mater.* **2009,** *57* (10), 2919-2932.

(6) Munch, E.; Launey, M. E.; Alsem, D. H.; Saiz, E.; Tomsia, A. P.; Ritchie, R. O. Tough, Bio-Inspired Hybrid Materials. *Science* **2008,** *322* (5907), 1516-1520.

(7) Kumar, S.; Ubaid, J.; Abishera, R.; Schiffer, A.; Deshpande, V. S. Tunable Energy Absorption Characteristics of Architected Honeycombs Enabled Via Additive Manufacturing. *ACS Applied Materials & Interfaces* **2019,** *11* (45), 42549-42560.

(8) Srinivasan, A.; Haritos, G.; Hedberg, F.; Jones, W. Biomimetics: Advancing Man-Made Materials through Guidance from Nature-an Update. *Applied Mechanics Reviews* **1996,** *49* (10S), S194-S200.

(9) Wegst, U. G.; Bai, H.; Saiz, E.; Tomsia, A. P.; Ritchie, R. O. Bioinspired Structural Materials. *Nature materials* **2015,** *14* (1), 23-36.

(10) Dunlop, J. W.; Fratzl, P. Biological Composites. *Annual Review of Materials Research* **2010,** *40*, 1-24.

(11) Martin, J. J.; Fiore, B. E.; Erb, R. M. Designing Bioinspired Composite Reinforcement Architectures Via 3d Magnetic Printing. *Nature Communications* **2015,** *6* (1), 1-7.

(12) Bonderer, L. J.; Studart, A. R.; Gauckler, L. J. Bioinspired Design and Assembly of Platelet Reinforced Polymer Films. *Science* **2008,** *319* (5866), 1069-1073.

(13) Krauss, S.; Monsonego-Ornan, E.; Zelzer, E.; Fratzl, P.; Shahar, R. Mechanical Function of a Complex Three-Dimensional Suture Joining the Bony Elements in the Shell of the Red-Eared Slider Turtle. *Adv. Mater.* **2009,** *21* (4), 407-412.

(14) Sun, J.; Bhushan, B. Hierarchical Structure and Mechanical Properties of Nacre: A Review. *Rsc Advances* **2012,** *2* (20), 7617-7632.

(15) Rabiei, R.; Bekah, S.; Barthelat, F. Failure Mode Transition in Nacre and Bone-Like Materials. *Acta Biomaterialia* **2010,** *6*, 4081-4089.

(16) Jackson, A. P.; Vincent, J. F. V.; Turner, R. M. The Mechanical Design of Nacre. *Proceedings of the Royal Society B: Biological Sciences* **1988,** *234*, 415-440.

(17) Wang, J.; Cheng, Q.; Tang, Z. Layered Nanocomposites Inspired by the Structure and Mechanical Properties of Nacre. *Chem. Soc. Rev.* **2012,** *41*, 1111-1129.

(18) Kakisawa, H.; Sumitomo, T. The Toughening Mechanism of Nacre and Structural Materials Inspired by Nacre. *Science and Technology of Advanced Materials* **2012,** *12* (6), 064710.

(19) Luz, G. M.; Mano, J. F. Biomimetic Design of Materials and Biomaterials Inspired by the Structure of Nacre. *Philosophical Transactions of the Royal Society of London A: Mathematical, Physical and Engineering Sciences* **2009,** *367* (1893), 1587-1605.

(20) Djumas, L.; Molotnikov, A.; Simon, G. P.; Estrin, Y. Enhanced Mechanical Performance of Bio-Inspired Hybrid Structures Utilising Topological Interlocking Geometry. *Scientific Reports* **2016,** *6*, 26706.

(21) Nalla, R.; Kinney, J.; Ritchie, R. Effect of Orientation on the in Vitro Fracture Toughness of Dentin: The Role of Toughening Mechanisms. *Biomaterials* **2003,** *24* (22), 3955-3968.

(22) Meyers, M. A.; Chen, P.-Y.; Lin, A. Y.-M.; Seki, Y. Biological Materials: Structure and Mechanical Properties. *Prog. Mater Sci.* **2008,** *53* (1), 1-206.

(23) Barthelat, F. Designing Nacre-Like Materials for Simultaneous Stiffness, Strength and Toughness: Optimum Materials, Composition, Microstructure and Size. *J. Mech. Phys. Solids* **2014,** *73*, 22-37.

(24) Kruzic, J. J.; Nalla, R. K.; Kinney, J. H.; Ritchie, R. Crack Blunting, Crack Bridging and Resistance-Curve Fracture Mechanics in Dentin: Effect of Hydration. *Biomaterials* **2003,** *24* (28), 5209-5221.

(25) Dastjerdi, A. K.; Rabiei, R.; Barthelat, F. The Weak Interfaces within Tough Natural Composites: Experiments on Three Types of Nacre. *Journal of the mechanical behavior of biomedical materials* **2013,** *19*, 50-60.

(26) Zhang, N.; Yang, S.; Xiong, L.; Hong, Y.; Chen, Y. Nanoscale Toughening Mechanism of Nacre Tablet. *Journal of the mechanical behavior of biomedical materials* **2016,** *53*, 200-209.

(27) Tang, Z.; Kotov, N. A.; Magonov, S.; Ozturk, B. Nanostructured Artificial Nacre. *Nature materials* **2003,** *2* (6), 413-418.

(28) Bentov, S.; Zaslansky, P.; Al-Sawalmih, A.; Masic, A.; Fratzl, P.; Sagi, A.; Berman, A.; Aichmayer, B. Enamel-Like Apatite Crown Covering Amorphous Mineral in a Crayfish Mandible. *Nature communications* **2012,** *3*, 839.

(29) Bruet, B. J.; Song, J.; Boyce, M. C.; Ortiz, C. Materials Design Principles of Ancient Fish Armour. *Nature materials* **2008,** *7* (9), 748.

(30) Bar-On, B.; Barth, F. G.; Fratzl, P.; Politi, Y. Multiscale Structural Gradients Enhance the Biomechanical Functionality of the Spider Fang. *Nature Communications* **2014,** *5*, 3894.

(31) Holten-Andersen, N.; Fantner, G. E.; Hohlbauch, S.; Waite, J. H.; Zok, F. W. Protective Coatings on Extensible Biofibres. *Nature materials* **2007,** *6* (9), 669.

(32) Harrington, M. J.; Masic, A.; Holten-Andersen, N.; Waite, J. H.; Fratzl, P. Iron-Clad Fibers: A Metal-Based Biological Strategy for Hard Flexible Coatings. *Science* **2010,** *328* (5975), 216-220.

(33) Wang, B.; Yang, W.; McKittrick, J.; Meyers, M. A. Keratin: Structure, Mechanical Properties, Occurrence in Biological Organisms, and Efforts at Bioinspiration. *Prog. Mater Sci.* **2016,** *76*, 229-318.

(34) Kasapi, M. A.; Gosline, J. M. Design Complexity and Fracture Control in the Equine Hoof Wall. *J. Exp. Biol.* **1997,** *200* (11), 1639-1659.

(35) Miserez, A.; Li, Y.; Waite, J. H.; Zok, F. Jumbo Squid Beaks: Inspiration for Design of Robust Organic Composites. *Acta Biomaterialia* **2007,** *3* (1), 139-149.

(36) Miserez, A.; Schneberk, T.; Sun, C.; Zok, F. W.; Waite, J. H. The Transition from Stiff to Compliant Materials in Squid Beaks. *Science* **2008,** *319* (5871), 1816-1819.

(37) Espinosa, H. D.; Juster, A. L.; Latourte, F. J.; Loh, O. Y.; Gregoire, D.; Zavattieri, P. D. Tablet-Level Origin of Toughening in Abalone Shells and Translation to Synthetic Composite Materials. *Nature communications* **2011,** *2*, 173.

(38) Wang, L.; Lau, J.; Thomas, E. L.; Boyce, M. C. Co-Continuous Composite Materials for Stiffness, Strength, and Energy Dissipation. *Adv. Mater.* **2011,** *23* (13), 1524-1529.

(39) Wegst, U. G.; Schecter, M.; Donius, A. E.; Hunger, P. M. Biomaterials by Freeze Casting. *Philosophical Transactions of the Royal Society of London A: Mathematical, Physical and Engineering Sciences* **2010,** *368* (1917), 2099-2121.

(40) Mao, L.-B.; Gao, H.-L.; Yao, H.-B.; Liu, L.; Cölfen, H.; Liu, G.; Chen, S.-M.; Li, S.-K.; Yan, Y.-X.; Liu, Y.-Y. Synthetic Nacre by Predesigned Matrix-Directed Mineralization. *Science* **2016,** *354* (6308), 107-110.

(41) Gao, H.-L.; Chen, S.-M.; Mao, L.-B.; Song, Z.-Q.; Yao, H.-B.; Cölfen, H.; Luo, X.-S.; Zhang, F.; Pan, Z.; Meng, Y.-F. Mass Production of Bulk Artificial Nacre with Excellent Mechanical Properties. *Nature communications* **2017,** *8* (1), 287.

(42) Sommer, M. R.; Schaffner, M.; Carnelli, D.; Studart, A. R. 3d Printing of Hierarchical Silk Fibroin Structures. *ACS Applied Materials & Interfaces* **2016,** *8* (50), 34677-34685.

(43) Studart, A. R. Additive Manufacturing of Biologically-Inspired Materials. *Chem. Soc. Rev.* **2016,** *45*, 359-376.

(44) Patole, S. P.; Reddy, S. K.; Schiffer, A.; Askar, K.; Prusty, B. G.; Kumar, S. Piezoresistive and Mechanical Characteristics of Graphene Foam Nanocomposites. *ACS Applied Nano Materials* **2019,** *2* (3), 1402-1411.

(45) Du, G.; Mao, A.; Yu, J.; Hou, J.; Zhao, N.; Han, J.; Zhao, Q.; Gao, W.; Xie, T.; Bai, H. Nacre-Mimetic Composite with Intrinsic Self-Healing and Shape-Programming Capability. *Nature communications* **2019,** *10* (1), 1-8.

(46) Han, J.; Du, G.; Gao, W.; Bai, H. An Anisotropically High Thermal Conductive Boron Nitride/Epoxy Composite Based on Nacre-Mimetic 3d Network. *Adv. Funct. Mater.* **2019,** *29* (13), 1900412.

(47) Budarapu, P.; Thakur, S.; Kumar, S.; Paggi, M. Micromechanics of Engineered Interphases in Nacre-Like Composite Structures. *Mechanics of Advanced Materials and Structures* **2020**, 1-16.

(48) Ubaid, J.; Wardle, B. L.; Kumar, S. Strength and Performance Enhancement of Multilayers by Spatial Tailoring of Adherend Compliance and Morphology Via Multimaterial Jetting Additive Manufacturing. *Scientific Reports* **2018,** *8* (1), 13592.

(49) Dugbenoo, E.; Arif, M. F.; Wardle, B. L.; Kumar, S. Enhanced Bonding Via Additive Manufacturing-Enabled Surface Tailoring of 3d Printed Continuous-Fiber Composites. *Adv. Eng. Mater.* **2018,** *20* (12), 1800691.

(50) Yadav, R.; Naebe, M.; Wang, X.; Kandasubramanian, B. Review on 3d Prototyping of Damage Tolerant Interdigitating Brick Arrays of Nacre. *Industrial & Engineering Chemistry Research* **2017,** *56* (38), 10516-10525.

(51) Saha, S. K.; Wang, D.; Nguyen, V. H.; Chang, Y.; Oakdale, J. S.; Chen, S.-C. Scalable Submicrometer Additive Manufacturing. *Science* **2019,** *366* (6461), 105-109.

(52) Vyatskikh, A.; Delalande, S.; Kudo, A.; Zhang, X.; Portela, C. M.; Greer, J. R. Additive Manufacturing of 3d Nano-Architected Metals. *Nature Communications* **2018,** *9* (1), 593.

(53) Dimas, L. S.; Bratzel, G. H.; Eylon, I.; Buehler, M. J. Tough Composites Inspired by Mineralized Natural Materials: Computation, 3d Printing, and Testing. *Adv. Funct. Mater.* **2013,** *23*, 4629-4638.

(54) Sakhavand, N.; Shahsavari, R. Universal Composition–Structure–Property Maps for Natural and Biomimetic Platelet–Matrix Composites and Stacked Heterostructures. *Nature communications* **2015,** *6* (1), 1-13.

(55) Zhang, P.; Heyne, M. A.; To, A. C. Biomimetic Staggered Composites with Highly Enhanced Energy Dissipation: Modeling, 3d Printing, and Testing. *J. Mech. Phys. Solids* **2015,** *83*, 285-300.

(56) Gu, G. X.; Takaffoli, M.; Buehler, M. J. Hierarchically Enhanced Impact Resistance of Bioinspired Composites. *Adv. Mater.* **2017,** *29* (28), 1700060.

(57) Khan, M. A.; Kumar, S.; Reddy, J. N. Material-Tailored Adhesively Bonded Multilayers: A Theoretical Analysis. *International Journal of Mechanical Sciences* **2018,** *148*, 246-262.

(58) Kumar, S.; Adams, R. D., Special Issue on Functionally Graded Adhesively Bonded Systems. Elsevier: 2017.

(59) Yang, Y.; Li, X.; Chu, M.; Sun, H.; Jin, J.; Yu, K.; Wang, Q.; Zhou, Q.; Chen, Y. Electrically Assisted 3d Printing of Nacre-Inspired Structures with Self-Sensing Capability. *Science advances* **2019,** *5* (4), eaau9490.

(60) Frølich, S.; Weaver, J. C.; Dean, M. N.; Birkedal, H.; Frølich, B. S.; Weaver, J. C.; Dean, M. N.; Birkedal, H. Uncovering Nature's Design Strategies through Parametric Modeling, Multi-Material 3d Printing, and Mechanical Testing. *Adv. Eng. Mater.* **2017**, 1-8.

(61) Parker, M. Mollusc-Inspired 3d-Printed Smart Helmets. *Nature Electronics* **2019,** *2* (5), 175.

(62) Yin, Z.; Hannard, F.; Barthelat, F. Impact-Resistant Nacre-Like Transparent Materials. *Science* **2019,** *364* (6447), 1260-1263.

(63) Grossman, M.; Bouville, F.; Masania, K.; Studart, A. R. Quantifying the Role of Mineral Bridges on the Fracture Resistance of Nacre-Like Composites. *Proceedings of the National Academy of Sciences* **2018,** *115* (50), 12698-12703.

(64) Peng, J.; Cheng, Q. Smart Nacre-Inspired Nanocomposites. *ChemPhysChem* **2018,** *19* (16), 1980-1986.

(65) X. Gu, G.; Su, I.; Sharma, S.; Voros, J. L.; Qin, Z.; Buehler, M. J. Three-Dimensional-Printing of Bio-Inspired Composites. *Journal of Biomechanical Engineering* **2016,** *138*, 021006.

(66) Begley, M. R.; Philips, N. R.; Compton, B. G.; Wilbrink, D. V.; Ritchie, R. O.; Utz, M. Micromechanical Models to Guide the Development of Synthetic 'Brick and Mortar'composites. *J. Mech. Phys. Solids* **2012,** *60* (8), 1545-1560.

(67) Stratasys Connex3 Objet260. https://www.stratasys.com/ (accessed April, 29).

Supplementary Information

Supplementary information includes material characterization of additively manufactured materials, geometric and material architecture of the nacreous structure, mechanical performance of ungraded nacreous structures, and performance comparison of baseline and graded nacreous structures, including synchronized video of load-displacement curves (Supplementary Video 1).

Funding Sources

Abu Dhabi National Oil Company (Award No: EX2016-000010)

Acknowledgements

Authors gratefully acknowledge financial support from the ADNOC under Award No: EX2016-000010.

Author contributions

S. Kumar conceived the idea. J. Ubaid fabricated samples via 3D printing, performed FE analysis and conducted experiments. S. Kumar and B.L. Wardle guided the project. All authors discussed the results and contributed to manuscript preparation.

Data availability

The data that support the findings of this study are available from the authors on request.

Competing Interests statement

Authors declare no competing financial or non-financial interests.

ToC Entry

The study demonstrates through experiments (enabled via multi-material additive manufacturing) and computations that compliance grading motifs in the mortar of nacre with optimal spatial gradients, apart from the bulk property mismatch between the brick and mortar and periodic architecture, can allow nacreous materials to be engineered with strong, tough, and damage tolerant properties.

ToC Graphic

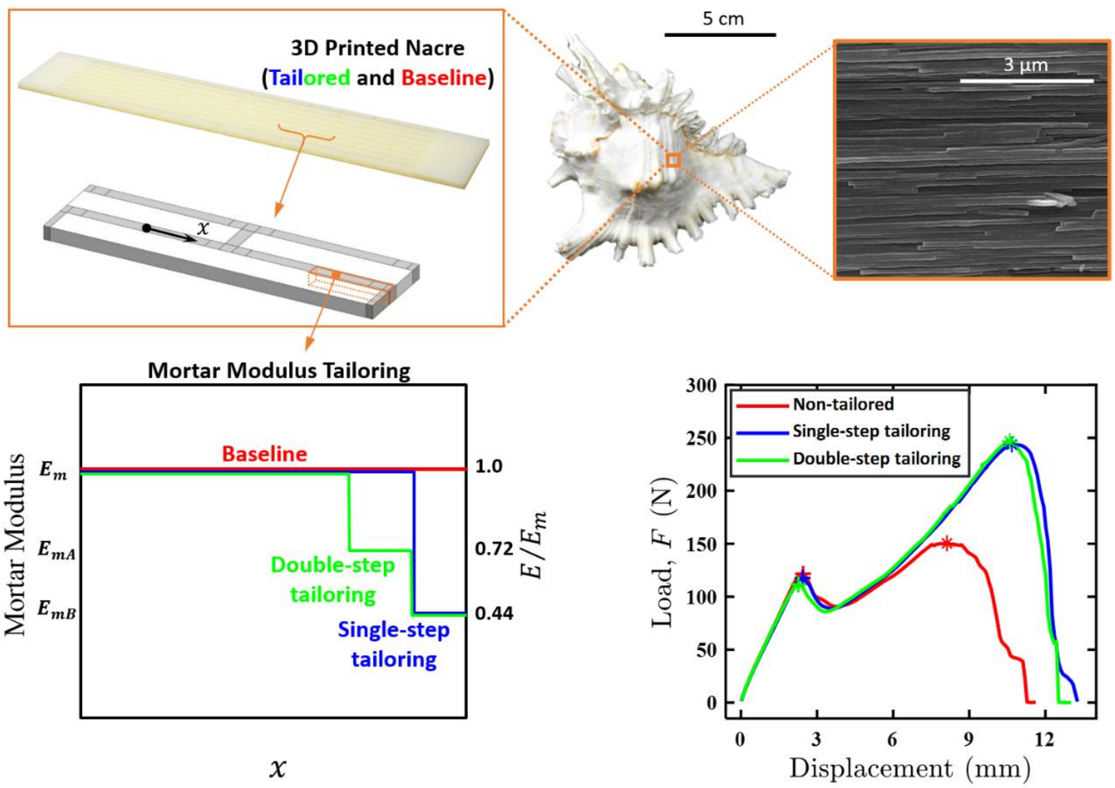

Figures

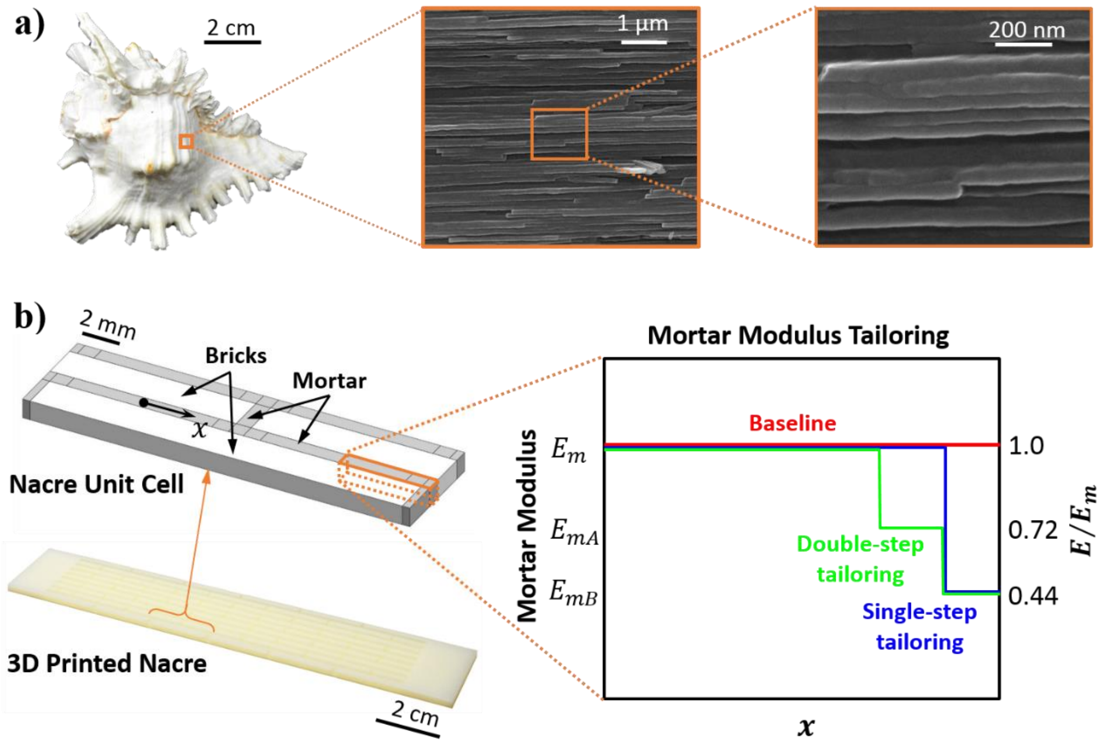

Figure 1. Nacre and its model showing the brick-and-mortar architecture: (a) Shell of ramose murex with SEMs of cross-section showing brick structure, and (b) 3D printed nacreous structure and unit cell of model indicating region of mortar modulus tailoring.

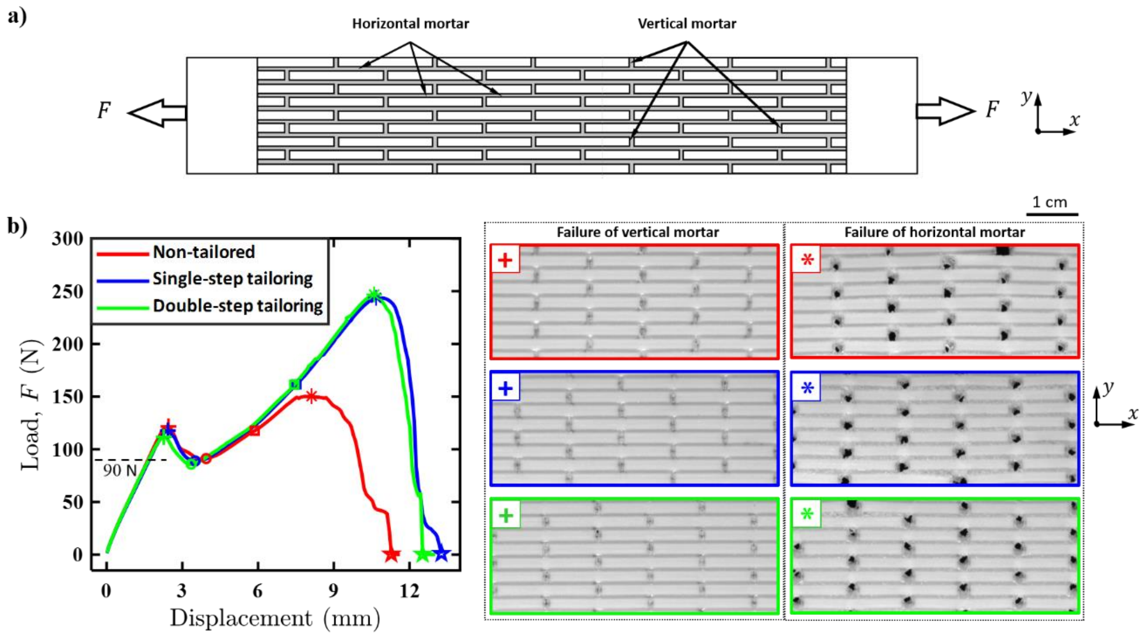

Figure 2. Performance comparison of baseline and tailored nacreous structures: (a) Schematic illustration of test specimen, (b) Representative load-displacement response together with optical images of the samples that indicate failure of vertical mortar (indicated by the first peak in the load-displacement response) and failure of horizontal mortar (ultimate failure) indicated by the second peak in the load-displacement response.

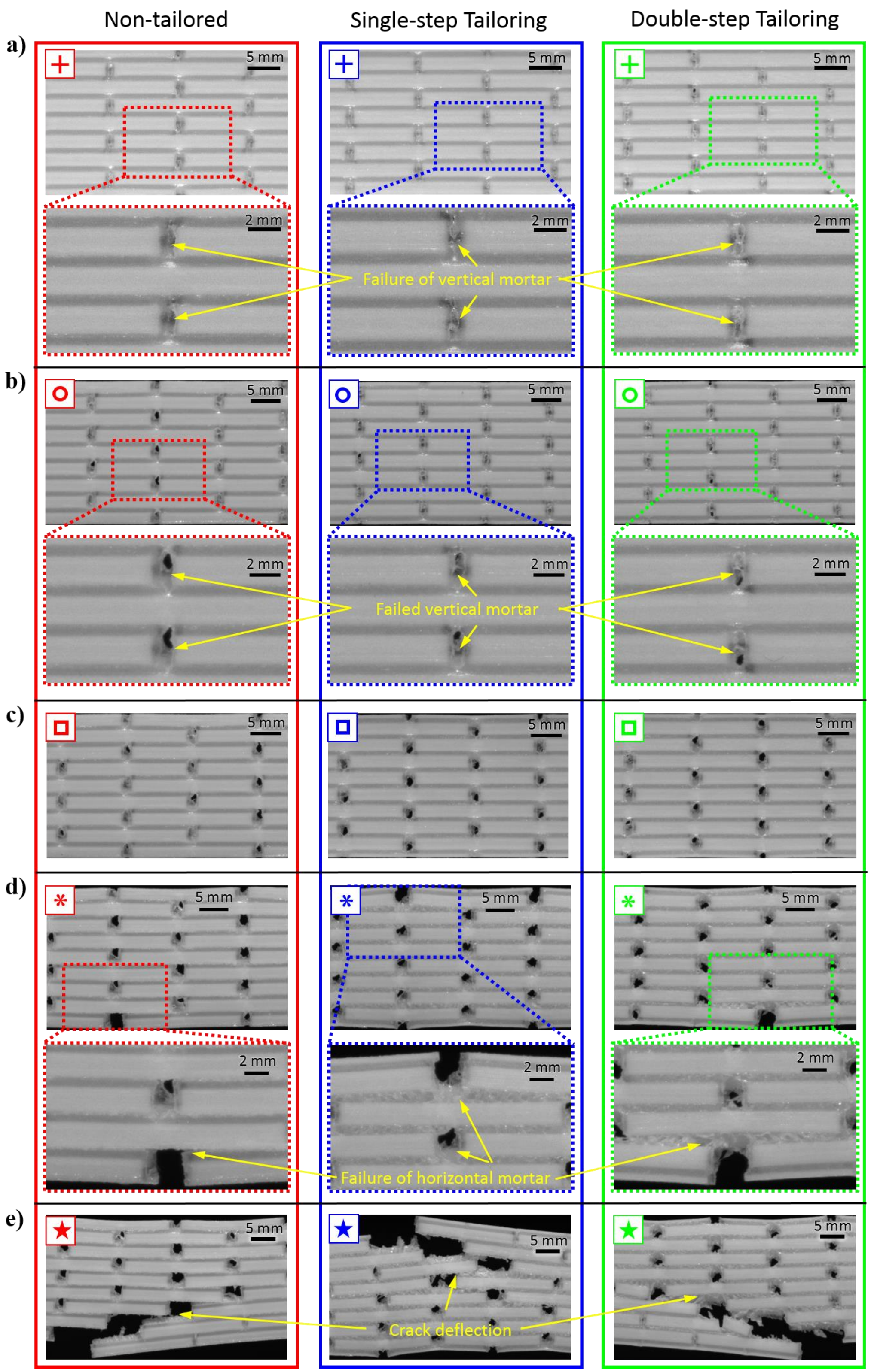

Figure 3. Optical images of deformation and failure behavior of AM-realized nacreous materials at different stages of loading (as indicated in the load-displacement response shown in Fig. 2a):

(a) failure of vertical mortar corresponding to the first peak in load-displacement response, (b) load transfer begins through horizontal mortar, (c) load is transferred wholly through horizontal mortar; damage evolution/growth in the horizontal mortar is clearly visible, (d) failure of horizontal mortar corresponding to second peak in load-displacement response and (e) final failure of structures exhibiting crack deflection.

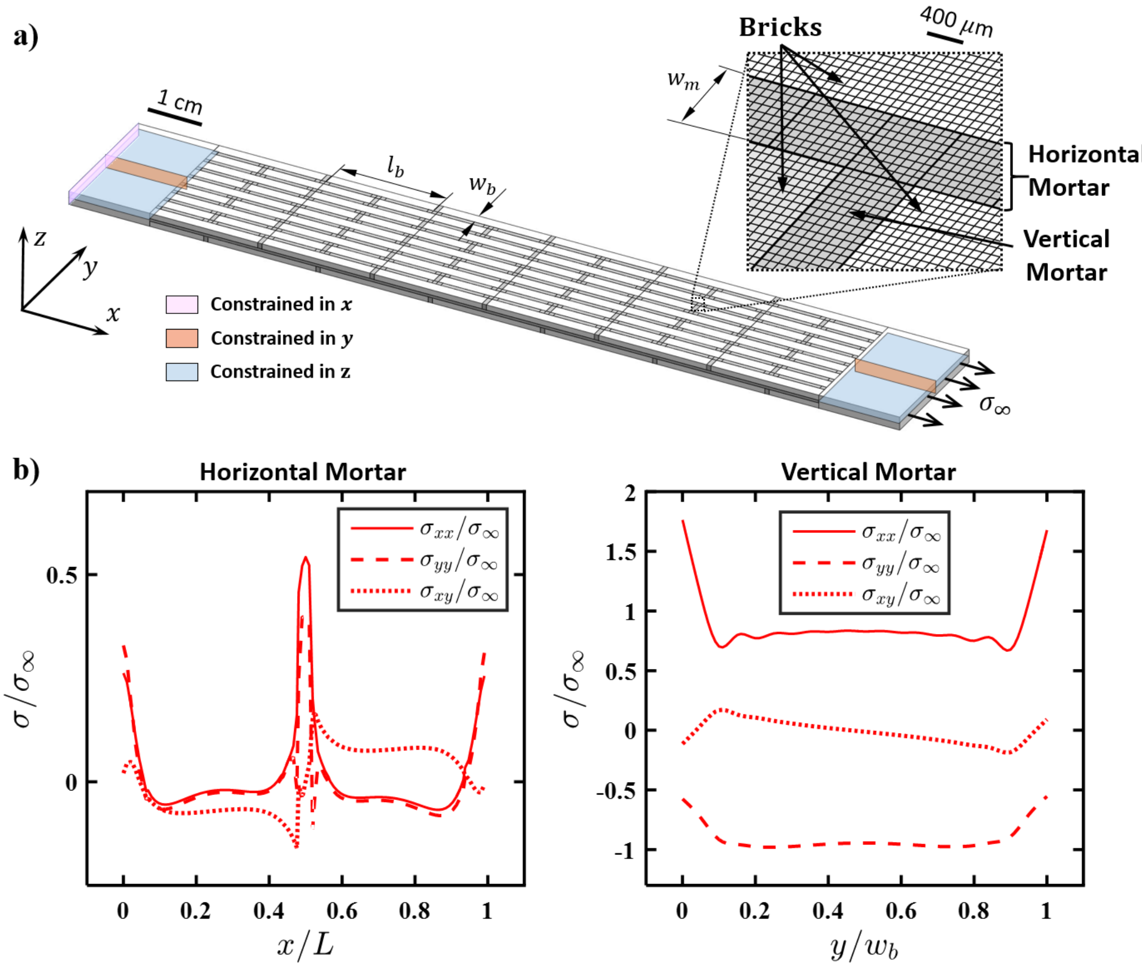

Figure 4. Finite element analysis of non-tailored (baseline) nacreous structures and stress distributions in the mortar: (a) Finite element model of the nacreous structure under far field stress σ_∞ and boundary conditions that replicate the mechanical testing scenario. Brick length, $l_b =$ 20 mm, brick width, $w_b = 2$ mm and the mortar thickness, $w_m = 0.8$ mm. The inset image shows mesh refinement near the brick edges where the stress concentrations arise. (b) Normalized longitudinal (σ_{xx}), peel (σ_{yy}) and shear stress (σ_{xy}) distributions in the horizontal and vertical mortars through the midline of a brick-mortar structure layer and near the brick mortar interface (0.15 mm from the interface) under a tensile load of 90 N (See Supplementary Fig. 7 for the lines of stress extraction).

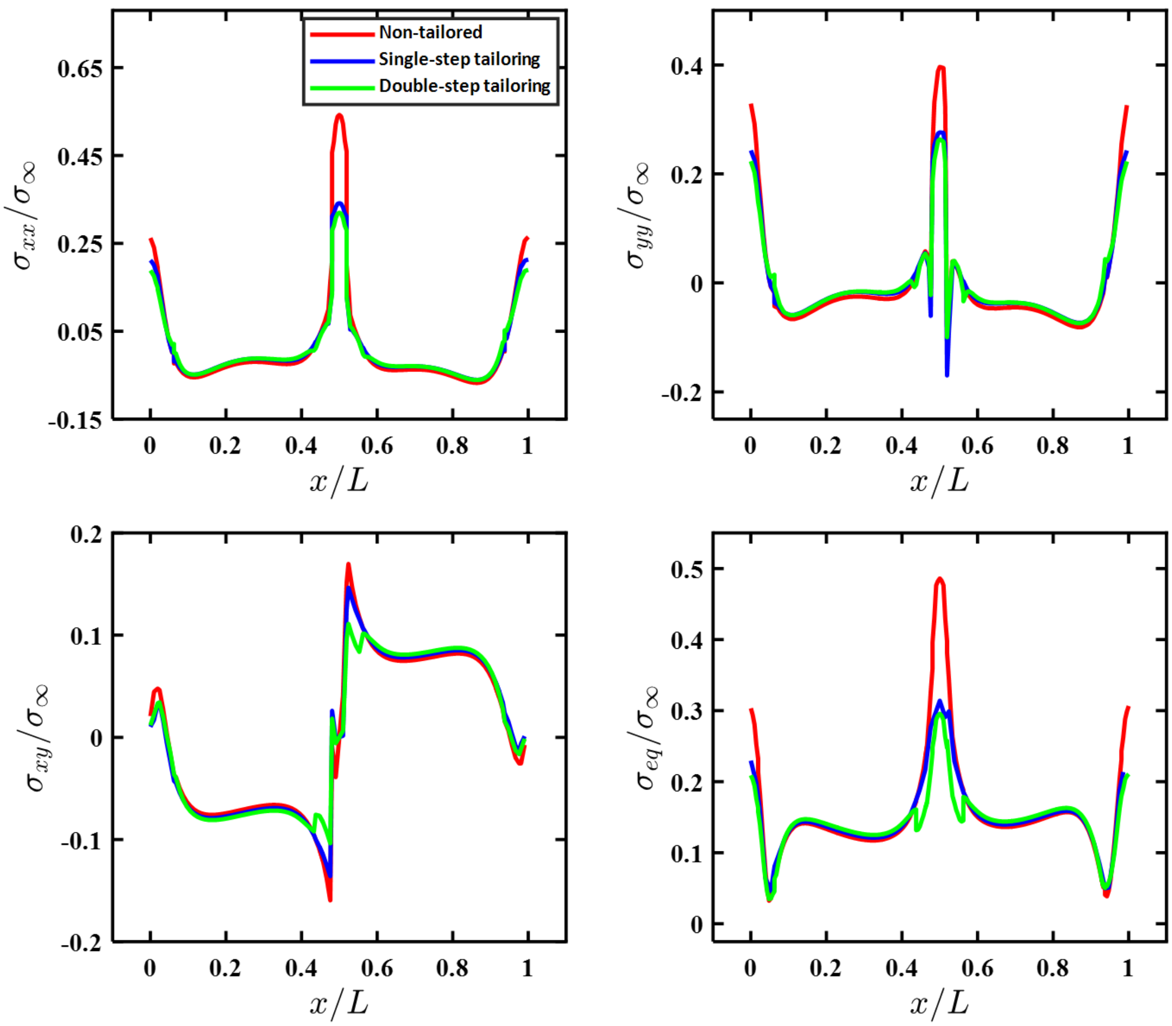

Figure 5. Normalized longitudinal (σ_{xx}), peel (σ_{yy}), shear stress (σ_{xy}) and equivalent stress (σ_{eq}) distributions in the horizontal mortar of the baseline and tailored structures over the length of a unit cell, at the layer midline of brick-mortar structure and near the brick-mortar interface (0.15 mm from the interface, see Supplementary Fig. 7) under a tensile load of 90 N (before the first peak load, see Fig. 2).

Tables

Table 1. Summary of the experimental performance of baseline and tailored nacreous AM structures with standard error. Significant changes from the baseline (non-tailored) case are shown in red.

Design Configuration	Initial stiffness (N/mm)	Load at first peak (N)	Maximum load (N)	Deflection at break (mm)	Modulus of toughness (Nm $\times 10^{-3}$)
Baseline	52.73 ± 0.44	121.69 ± 0.21	150.03 ± 0.35	8.12 ± 0.04	818.66 ± 0.28
Single-step tailoring	51.46 ± 0.78	117.76 ± 2.54 (-3.2%)	243.39 ± 3.12 (+62.2%)	10.67± 0.09 (+31.4%)	1375 ± 8.46 (+67.9%)
Double-step tailoring	52.32± 0.34	111.6 ± 0.97 (-8.3%)	246.76 ± 1.56 (+64.5%)	10.59 ± 0.09 (+30.4%)	1401.6 ± 7.21 (+71.2%)

Table 2. Summary of the stress peaks in baseline and tailored nacreous structures obtained from numerical analysis. Significant changes from the baseline (non-tailored) case are shown in red.

Design Configuration	Maximum longitudinal stress (MPa)	Maximum peel stress (MPa)	Maximum shear stress (MPa)
Baseline	0.542	0.397	0.169
Single-step tailoring	0.341 (-37 %)	0.277 (-30 %)	0.147 (-13 %)
Double-step tailoring	0.319 (-41 %)	0.263 (-34%)	0.111 (-34%)